The Cryosphere Discuss., 4, 2433–2473, 2010
www.the-cryosphere-discuss.net/4/2433/2010/
doi:10.5194/tcd-4-2433-2010

The Cryosphere Discussions

Melting trends over the Greenland ice sheet (1958–2009) from spaceborne microwave data and regional climate models

X. Fettweis[1,3], M. Tedesco[2], M. van den Broeke[3], and J. Ettema[3]

[1]Département de Géographie, Université de Liège, Liège, Belgium
[2]City College of New York, City University of New York, New York, NY, 10031, USA
[3]Institute for Marine and Atmospheric Research, Utrecht University, Utrecht, The Netherlands

Received: 25 October 2010 – Accepted: 8 November 2010 – Published: 15 November 2010

Correspondence to: X. Fettweis (xavier.fettweis@ulg.ac.be)

Published by Copernicus Publications on behalf of the European Geosciences Union.

Abstract

To study near-surface melt changes over the Greenland ice sheet (GrIS) since 1979, melt extent estimates from two regional climate models are compared with those obtained from spaceborne microwave brightness temperatures using two different remote sensing algorithms. Results from the two models are consistent with those obtained with the remote sensing algorithms, at both daily and yearly time scales, encouraging the use of the models for analyzing melting trends before the satellite era (1958–1979), when forcing data is available. Differences between satellite-derived and model-simulated results still occur and are here used to identify (i) biases in the snow models (notably in the albedo parametrization, in the thickness of a snow layer, in the maximum liquid water content within the snowpack and in the snowfall impacting the bare ice appearance in summer) and (ii) limitations in the use of passive microwave data for snowmelt detection at the edge of the ice sheet due to mixed pixel effect (e.g., tundra or rock nearby the ice sheet). Results from models and spaceborne microwave sensors confirm a significant (p-value = 0.01) increase in GrIS surface melting since 1979. Melt extent recorded over the last years (1998, 2003, 2005 and 2007) is unprecedented in the last 50 years with the cumulated melt area in the 2000's being, on the average, twice as that occurring during the 1980's.

1 Introduction

Melting over the Greenland ice sheet (GrIS) has been accelerating over the past decades, as suggested by recent satellite-based observations (Mote, 2007; Hall et al., 2008; Tedesco et al., 2008; Wouters et al., 2008) and model simulations (Fettweis, 2007; Hanna et al., 2008; Ettema et al., 2009; Van den Broeke et al., 2009). This can be partially attributed to recent observed warming of the Arctic, generally attributed to increases in atmospheric greenhouse gas loading (Hanna et al., 2008). Satellite based mass estimates began in the early 1990's with the European Remote-sensing (ERS)

TCD
4, 2433–2473, 2010

satellites (Zwally et al., 2005) followed by the NASA Gravity Recovery and Climate Experiment (GRACE) (Wouters et al., 2008) and, therefore, cannot capture long-term mass variations of the GrIS (also given the large inter-annual variability observed in the mass balance and surface melt).

Measurements from coastal weather stations managed by the Danish Meteorological Institute (DMI) are available for more than a century. However, in this case data are collected at local spatial scales and, therefore, cannot be assumed to be representative of other places (e.g., interior of the GrIS). Nevertheless, these data can be used to quantify the inter-annual variability (Fettweis et al., 2008; Wake et al., 2009) at selected locations. Results from regional climate models (RCMs) can provide estimates of GrIS surface changes over a long period at high resolution, but measurements to validate these models are limited.

With more than 30 years of data, the spaceborne passive microwave brightness temperature data set offers a unique opportunity to study changes of near surface melting over the GrIS (Abdalati and Steffen, 2001; Mote, 2007; Tedesco, 2007). When snow melts, the presence of liquid water within the snowpack increases the snow microwave emissivity (Ulaby and Stiles, 1980). Consequently, microwave brightness temperatures (e.g., the product of snow temperature and emissivity) are considerably higher in the case of wet snow than those in the case of dry snow and several algorithms have been developed to detect melting from spaceborne passive microwave data (Abdalati and Steffen, 1997; Picard and Fily, 2006; Mote, 2007; Tedesco, 2007).

Combining results from modeling and measurement tools (e.g., satellite data) would provide an ideal framework to overcome some of the intrinsic limitations of each tool considered separately. In this study, we analyze results from two Regional Climate Models (RCMs) in conjunction with those obtained from spaceborne microwave brightness temperatures to study surface and near-surface melt over the GrIS since 1979 and, extend the analysis back to 1958. A major outcome from this study is a first assessment of the potential assimilation of melt detection from spaceborne microwave data into the RCMs, with the ultimate scope of reducing uncertainties in model-based

TCD
4, 2433–2473, 2010

Surface Mass Balance (SMB) estimates. The RCMs used in this study are MAR (for Modèle Atmosphérique Régional) described by Gallée and Schayes (1994) and Fettweis (2007) and, RACMO2 described by Ettema et al. (2009). Both RCMs are fully coupled with an energy balance-based snow model allowing feedbacks between surface and atmosphere. The models are forced at the boundaries by the re-analyses of the European Centre for Medium-Range Weather Forecasts (ECMWF) since September 1957. Both models have demonstrated their ability to reliably simulate the GrIS SMB since 1958 (Ettema et al., 2009; Fettweis et al., 2010). The MAR model was already satisfactorily compared with passive microwave-derived observations (Fettweis et al., 2005, 2007) and was used to improve the microwave-based algorithm developed by Abdalati and Steffen (2001) for retrieving melt extent (Fettweis et al., 2006).

This study complements a previously published study of Fettweis et al. (2007) by using two different RCMs outputs rather than only MAR, hence allowing a more robust analysis, especially in those cases when results from models and remote sensing algorithms data are not consistent. The data used are described in Sect. 2. In Sect. 3, two space-borne passive microwave melt retrieval techniques are discussed and their results compared with in-situ measurements. In Sect. 4, RCMs outputs are used to assess the applicability of these algorithms over areas and periods where no measurements are available. Finally, in Sect. 5, the melting variability is estimated before the beginning of satellite observations using the two models. The aims of this paper are triple: (i) to select melt retrieval algorithms that can be easily compared with RCM outputs, (ii) to inter-validate both RCMs and the satellite-retrived melt extent and, (iii) to show the unprecedented behavior since 50 years of the last years melt extent.

2 Data

Satellite data consist of spaceborne passive microwave brightness temperatures recorded by the Scanning Multichannel Microwave Radiometer (SMMR) satellite (1979–1987), the Special Sensor Microwave/Imager (SSM/I) flying on the

TCD
4, 2433–2473, 2010

F-08 (1987–1991), F-11 (1992–1994) and F-13 (1995–2009) satellites and by the Special Sensor Microwave Imager/Sounder (SSMIS) on the F-17 satellites (2009). Microwave data are available at four frequencies: 18.7 GHz (respectively 19.35 GHz for SSM/I(S) data) at both vertical (V) and horizontal (H) polarizations, 22.2 (V), 37.0 (V, H) and, 85.5 GHz (V, H). Data are re-projected on a 25 km × 25 km grid (EASE-Grid) and distributed by the National Snow and Ice Data Center (NSIDC, Boulder, Colorado) (Armstrong et al., 1994, Knowles et al., 2002). We use the near-real time SSMI/S brightness temperatures after May 2009 (Brodzik and Armstrong, 2008). Data acquired during both ascending and descending passes are averaged to generate daily values of brightness temperature, as in Abdalati and Steffen (1997, 2001). In addition, data gaps for periods shorter than three days are filled through linear interpolation.

MAR outputs are available at 25 km horizontal resolution (1958–2009) using the same model set-up described by Fettweis (2007) and with improvements in the surface albedo scheme after Fettweis et al. (2010). First comparisons between the modeled and satellite-derived melt extent using results of the previous MAR version highlighted some biases in the MAR surface albedo scheme which are now corrected for the results presented here. For RACMO2, we use the 11 km-results from Ettema et al. (2009, 2010) without changes. The atmospheric modules of MAR and RACMO2 (atmospheric dynamics, micro-physics, turbulence scheme, etc.) are of similar complexity. Both RCMS are fully coupled with a multi-layered energy balance snow model taking into account the meltwater percolation, retention and refreezing, the bare ice presence, the increase in snow density due to refreezing of liquid water and the packing of dry snow. Only the surface albedo scheme is rather different. In RACMO2, albedo is a simple function of the snow density and cloudiness (Greuell and Konzelmann, 1994) while in MAR it depends on the shape and size of the snow grains (following the CROCUS snow albedo parametrization developed by Brun et al., 1992), on the cloudiness and on the zenithal angle (Lefebre et al., 2003).

Results from RACMO2 and satellite data are re-projected on the 25 km MAR grid using an inverse distance weighted interpolation. Ice sheet masks for the three different

TCD
4, 2433–2473, 2010

data sets are saved and the analysis is performed only over those pixels where the ice sheet is assumed to be present on all of the three different ice masks. For the spaceborne passive microwave data set, we use the ice mask from the EASE-Grid LOCI mask (derived from Boston University Version of Global 1 km Land Cover from MODIS (Moderate Resolution Imaging Spectroradiometer) 2001, Version 4). Finally, ice pixels along the coast are excluded from our analysis in order to reduce the uncertainty related to sea ice/ocean mixed pixel effect.

3 Satellite-based algorithms for melt detection

Several approaches have been proposed for mapping wet snow over the Greenland and Antarctica ice sheets from spaceborne passive microwave measurements. Most of them use data collected at K-band (18.7 GHz for SMMR and 19.35 GHz for SSM/I(S) data) horizontal polarization (T19H) because of the largest observed difference of this combination of frequency and polarization between dry and wet snow conditions (e.g. Liu et al., 2006, Tedesco, 2007). The two main methods for wet snow detection are either the use of a threshold value of T19H (or a combination of brightness temperatures)as following

$$\begin{cases} \text{Melt if} \quad T19H \geq T19H_{thsd} \\ \text{No Melt if} \quad T19H < T19H_{thsd} \end{cases} \tag{1}$$

or the tracking of steep rises and drops in the brightness temperature time series (corresponding to the onset and respectively the end of a melt event) for delimiting the melting periods. With this last approach, a pixel is detected as melting for those days included between a successive upward and downward edge pair in the time series (Joshi et al., 2001; Liu et al., 2006). In this paper, however, we will specifically focus on algorithms based on the use of a threshold value.

TCD
4, 2433–2473, 2010

3.1 Methodology

1. The most elementary approach to detect the presence of meltwater within the snowpack is to use a spatially and temporally fixed threshold value of $T19H_{thsd}$ in Eq. (1) over the entire GrIS. The threshold value can be estimated either from theoretical considerations or from the comparison between satellite data and ground observations.

2. Several authors (Zwally and Fiegles, 1994; Torinesi et al., 2003; Picard and Fily, 2006; Tedesco, 2009) proposed an adaptive T19H-threshold using the mean brightness temperature over the previous cold season ($\overline{T19H}_{cold\,season}$) plus a $\Delta T19H$ as following:

$$T19H_{thsd} = \overline{T19H}_{cold\,season} + \Delta T19H \quad (2)$$

This $\Delta T19H$ can be fixed (e.g. Zwally and Fiegles, 1994; Tedesco, 2009) or proportional to the winter T19H standard deviation (Picard and Fily, 2006). Differences in the $\Delta T19H$ values account for the different sensitivities of the algorithms to the minimum amount of liquid water content within the snowpack.

3. Mote (2007) used a microwave-emission model to determine the T19H threshold associated with a 1% volumetric water content for each grid cell and each year over the GrIS.

4. Abdalati and Steffen (2001) proposed a method based on a combination of the K-band horizontal polarized brightness temperature (T19H) and the Ka-band (36.5 GHz) vertical polarized brightness temperature (T37V) (called cross-polarized gradient ratio, XPGR) to detect liquid water:

$$XPGR = \frac{T19H - T37V}{T19H + T37V} \quad (3)$$

TCD
4, 2433–2473, 2010

An XPGR threshold value ($XPGR_{thsd}$) is defined to separate pixels containing wet snow from those with dry snow. The threshold values were originally determined by comparing XPGR values to the liquid water content (LWC) of the snowpack at the ETH-Camp (West-Greenland, 69.6° N, 49.2° W) during the 1990 and 1991 melting seasons and correspond approximately to a LWC of 1% by volume in the top meter of snow (Abdalati and Steffen, 1997). Bare ice (melting or not) in the ablation zone is also detected as melting by XPGR. The XPGR threshold varies with the spaceborne passive microwave sensors according to Abdalati and Steffen (2001). According to (Abdalati and Steffen, 2001), the XPGR algorithm is sensitive to (sub-)surface melting and to the presence of liquid water in the snowpack when the snow is refreezing at the surface at the end of the summer.

In the following, we discuss more in details some of the above-mentioned algorithms.

3.2 Algorithms discussion

3.2.1 Constant T19H melt threshold

A source of uncertainty when using Eq. (1) with a constant threshold is related to the different satellites passing times and cross-calibration of sensors (Picard and Fily, 2006). For example, for those areas where refreezing occurs at night, the use of daily mean brightness temperature values might affect retrieval performances, depending on which sensor is used: if the ascending and descending passes occur around local midnight and noon (as in the case of SMMR) then the mean daily brightness temperature could be lower than that computed using data collected around 06:00 a.m. and 06:00 p.m. (as for the SSM/I) when brightness temperature reaches its maximum (Picard and Fily, 2006). The SSM/I sensors (F08, F11, F13, F17, we will refer here as SSM/I to both SSM/I and SSMIS sensors) indeed collect data over the GrIS in early morning during descending orbit and in the late afternoon during ascending orbit (there is a shift of 1 or 2 h between the different SSM/I sensors). The difference between SSM/I and SMMR

TCD
4, 2433–2473, 2010

passing time can be a relevant issue, especially at the beginning and at the end of the melting season, when melting may be lasting only a few hours during the mid to late afternoon. The difference between brightness temperatures collected during ascending and descending passes (diurnal amplitude variations = DAV) can also be used to detect early and late melt in the season (Tedesco, 2007). Over the SMMR period, the DAV-based technique using a static DAV threshold value might not work properly (Fig. 1) because the acquisition hours between SMMR and SSM/I are shifted by about 7 h and the mean DAV is much lower for the SMMR sensor. Moreover, over the ice sheet, there is often a delay of 2–3 h in the acquisition time between the western and the eastern coasts. Therefore a dynamic approach when using DAV should be adopted (Tedesco et al., 2010).

A simple solution to reduce the impact of using a constant threshold in Eq. (1) over the whole SMMR-SSM/I covered period is to cross-calibrate the five sensors (for example by computing a linear regression of the brightness temperatures over a common period covered by any two sensors, Abdalati et al., 1995). One month at least of common data is available for the several sensors (1987, 1991, 1995, 2009). The five sensors are cross-calibrated to the F8 baseline as in (Abdalati and Steffen, 2001) and in (Liu et al., 2006) and only the GrIS pixels are retained here for the inter-calibration.

With the objective to homogenize the SMMR-SSM/I data set, Picard and Fily (2006) proposed a methodology to estimate the diurnal cycle of the brightness temperatures from the two passes, by using time series acquired by four different microwave radiometers after 2002. However, uncertainties are still present notably due to differences in the spatial resolution used by the SMMR and SSM/I radiometers. Moreover, the interannual variations of the brightness temperatures daily amplitude is only known after 2002, which is not enough to apply reliably this methodology to the whole spaceborne passive microwave data set.

TCD
4, 2433–2473, 2010

3.2.2 Adaptive T19H melt threshold

Another solution to the problem of uncertainties linked to the sensors inter-calibration is the adoption of an adaptive T19H-threshold, re-computed every year. However, the approach of Picard and Fily (2006)

$$\Delta T19H = 2.5\sigma_{\overline{T19H}_{\text{cold season}}} \quad (4)$$

might overestimate melting over the dry snow zone, where the winter standard deviation ($\sigma_{\overline{T19H}_{\text{cold season}}}$) is very low. For example, the algorithm in object detects more than >100 days of melting at Summit (see Fig. 2) while no melting generally occurs at that location. If we increase the multiplicative factor (currently 2.5) in ΔT19H or if we use a fixed ΔT19H value (e.g. 30 K according to Zwally and Fiegles, 1994), the T19H-threshold becomes too high to detect melt in the ablation zone where the annual cycle is very small as pointed out by Mote and Anderson (1995).

3.2.3 Edges tracking in T19H time series

An edge-detection approach might be detecting melting events during winter as shown Fig. 2 where there are several significant changes in the KULU station winter time series not corresponding to a melt event in most of the cases (e.g. in December 1999 and 2001). The Automatic Weather Stations (AWS) KULU comes from the Greenland Climate Network (GC-Net) (Steffen and Box, 2001). Hoar, accumulation, wind direction and surface temperature variability can also induces large changes in the dry snow microwave emissivity (Bingham and Drinkwater, 2000). In addition, along the western ice sheet margin, the inter-annual variability is low and the melt season is not delimited by clear edges in the T19H time series.

TCD
4, 2433–2473, 2010

3.2.4 Microwave-emission model for estimating a T19H melt threshold

The methodology of Mote (2007) is less sensitive than other approaches to discrepancies due to changes in the passing time over the years and pixels because the microwave scattering coefficients of the snowpack are derived from the T19H at the beginning of every melt season. However, given the lack of data, several properties of the snowpack (temperature, density and grain size) are empirically derived and used in the retrieval, this being a source of uncertainty. Eventually, results from the RCMs could be used to take into account the inter-annual variability of the snowpack properties before the melt season in this algorithm.

3.2.5 XPGR-based melt detection

This approach uses multiple frequencies and polarizations to take advantage of their different responses to LWC increase within the snow pack. However, Fettweis et al. (2005, 2006, 2007) showed that the XPGR approach does not detect melt during rainfall events due to the use of the 37 GHz channel.

Consequently, Fettweis et al. (2006) proposed an improved version of XPGR (called ImpXPGR), imposing the continuity of the melt season to remove gaps shorter than three days between two melting days. These gaps are found to be associated with dense clouds, mostly causing liquid precipitation on the ice sheet. However, we have not enough in situ data to affirm that the melt season (presence of liquid meltwater) is continuous in time and therefore, this hypothesis needs to be further assessed.

3.3 Algorithms used in this study

3.3.1 T19H-based melt detection

Each of the methods discussed above has intrinsic limitations. In the following, we use the simplest algorithm (i.e. a constant T19H threshold) with cross-calibrated data. In the future, we plan to extend the analysis to other algorithms as well. As we will

TCD
4, 2433–2473, 2010

see in the next section, melt extent derived from Eq. (1) with a constant T19H threshold compares favorably with the RCMs over the full 1979–2009 period. This algorithm will be named T19Hmelt hereafter. The RCMs-based time series can be considered as quasi-homogeneous knowing that the RCMs are forced by the ERA-40 reanalysis (1977–2002) and after that by the ERA-Interim reanalysis (2002–2009) from the ECMWF.

The value of the T19H threshold is calculated by using near-surface temperature measurements performed by AWS of GC-Net between 1995 and 2005 (Steffen and Box, 2001). We assume that melt occurs if the daily mean near-surface temperature is above 0 °C. A different and more sensitive threshold for detecting near-surface melt could be calculated using the maximum 2-m temperature above 0 °C, as used by Torinesi et al. (2003). But melt occurs only if the surface temperature reaches the melting point for a period long enough whereas a positive maximum 2-m temperature does not necessarily induce surface melt in case of surface inversion or radiative heating of the sensor. A positive daily mean near-surface temperature suggests that the temperature was positive for a long period, indicating that near-surface melt is likely to occur.

Figure 3 shows time series of surface temperature simulated by the two RCM models (MAR and RACMO2) together with GC-Net measured surface/air temperature for the CP-1, Dye-2, ETH Camp and Jar1 GC-Net stations for selected years. For each station, the temporal trend of the K-band horizontally polarized brightness temperature is also presented. In this figure, for each station, we also show the temporal trend of the XPGR, together with a binary plot in which melting derived using different approaches is indicated by the value 1 and no-melting is indicated with a 0 value. We also compare near-surface temperature simulated by the RCMs with that measured at GC-Net stations. Over the period 1995–2005, the biases in modeled temperature are very low: MAR (resp. RACMO2) underestimates (resp. overestimates) the measured near-surface temperature by 0.04 °C (resp. 1.3 °C) (see Table 1).

We use two criteria for detecting melt in the RCM modeled time series (a list of the algorithms used to retrieve melt can be found in Table 2). The first one *(temp)* uses

TCD
4, 2433–2473, 2010

a positive daily mean 2 m-temperature as melt threshold and compares favorably with the GC-Net-based time series melt detection (see Table 1). The second approach *(melt)* uses modeled daily meltwater production as melt threshold and compares better on average with the T19H-derived melt time series, as we will see in the next section. The best agreement between the melt/no melt time series using observed daily mean temperature over the 20 GC-NET AWS listed by Steffen and Box (2001) and the melt time series derived from T19H by using Eq. (1) is obtained with $T19H_{thsd}=227.5\pm2.5$ K (see Table 3), with more than 95% of melt events detected. Figure 3 shows melt and temperature time series for four GC-Net AWS where considerable melting is recorded. We have selected in Fig. 3 four summers for four different AWS's where no gap is present in the data.

Obviously, it would be ideal to compare melt events detected with T19H time series with measurements of snow properties, in particular liquid water content (LWC), because the snowpack response to positive air temperatures is complex and melting is also depending on other factors, such as albedo, for example. Unfortunately, LWC is not recorded by the GC-Net AWS. Therefore, we use results from RCMs coupled with a snow model to refine our analysis.

The daily Eq. (1)-derived melt signal is compared for the 1979–2009 period with corresponding time series simulated by the models and applying different melt detection criteria based on a threshold using

- surface and near-surface temperature.
- internal snowpack temperature.
- LWC in the snowpack.
- presence of bare ice at the surface (surface snow density higher than 900 kg m^{-3}).
- meltwater run-off.
- meltwater production.

TCD
4, 2433–2473, 2010

The best comparison occurs for a production of daily meltwater (surface and subsurface) higher than 8.5 ± 0.75 mmWE day^{-1} in the models (see Table 4). Table 4 also lists the sensitivity of the meltwater threshold used in the RCMs to $T19H_{thsd}$. Model results suggest that the algorithms based on only the T19H are more sensitive to the production of near-surface meltwater, rather than the presence of liquid water (or bare ice) in the snowpack, as the algorithm developed by Abdalati and Steffen (1997). This suggests that the T19H-based algorithm might not detect melting at the end of the ablation season, when the surface is refreezing but liquid water may still be present in the snowpack or bare ice may appear on the surface. Unfortunately, no in-situ measurements are available to confirm this hypothesis. We use the same value of daily produced meltwater threshold for both RCMs, which reduces the uncertainty on the relation between $T19H_{thsd}$ and model-simulated daily meltwater production. Figure 4 shows that the choice of the value of the melt threshold could considerably influence the estimated melt extent area while the linear trends over 1979–2009 are similar. The comparison between model-simulated and satellite-derived melt extent is discussed in more detail in the next section.

3.3.2 XPGR-based melt detection

Based on the analysis of the remote sensing-based algorithms, we evaluate the outputs of a new approach, based on the merging of the XPGR algorithm of Abdalati and Steffen (2001) and Eq. (1) to give:

$$\begin{cases} \text{Melt if} \quad XPGR \geq XPGR_{thsd} \quad \text{or} \quad T19H \geq 227.5\,\text{K} \\ \text{No Melt if} \quad XPGR < XPGR_{thsd} \quad \text{and} \quad T19H < 227.5\,\text{K} \end{cases} \tag{5}$$

In this case, melting is considered to be occurring if either XPGR or T19H is higher than the corresponding threshold values. We point out that, as in Fettweis et al. (2006), 227.5 K (resp. 190 K) is close to the mean T19H temperature (= 225.3 K) plus half of the standard deviation (= 3.1 K) over 1979–2009 and over all pixels of the whole melt area where XPGR detects melting. This last addition to the XPGR algorithm corresponds to

TCD
4, 2433–2473, 2010

Correction #3 of ImpXPGR (see Fettweis et al. (2006) for more details). This improved version of XPGR will be called hereafter ExtXPGR for Extended XPGR.

In order, to compare the XPGR-like algorithms with RCM outputs, as melt threshold value above which the model indicates melting we use a modeled LWC higher than 1.2% in the top meter of snow, in conjunction with the hypothesis of a surface snow density greater than 900 kg m^{-3} for detecting bare ice. The value of 1.2% was chosen (instead of 1% as suggested by Abdalati and Steffen, 1997) because it compares better with the satellite-derived data set.

4 Melt extent analysis

Results from both models and satellites in Fig. 5 indicate that, on the average, the melting season begins in mid-May, culminates in mid-July (when the highest melt extent occurs on average) and lasts until the end of September (see Fig. 5), when melting is small or negligible. T he average maximum melt extent is between 15 and 20% of the GrIS area (~1.61 × 10^6 km^2). The mean correlation between the daily melt extent evolution simulated by the models and that derived from spaceborne microwave remote sensing observations is ~0.93 with the mean RMSE being ~3% of the ice sheet surface. In general, the agreement between model- and satellite-derived results is better during the years with low melting (the SMMR years, 1992, 1996) than during those years with high melting (2000's). For reader convenience, comparison between satellite and RCMs for each year between 1979 and 2009 are reported in the Supplementary material.

Areas with more than 100 melting days/summer in average lie below 70° N along the ice sheet margin and at the north-east of the ice sheet (Fig. 6). The melt season lasts generally longer in the South-West with more than four months of melt days detected by ExtXPGR, on average. Over the whole ice sheet, the average difference between the total mean number of melt days by summer simulated by the models and retrieved from satellite data with T19Hmelt (resp. ExtXPGR) is 2.5 days (resp. 4.5 days). In 95%

TCD
4, 2433–2473, 2010

of the cases, there is agreement on a pixel by pixel and day by day cases between RCMs and satellite-derived melt detected events.

The disagreement between satellite and models can be due to (i) limitations in the algorithms used to derive the melt extent from the microwave data set but also to (ii) biases in the models. The error bars show that using a melt threshold slightly different on both models and on the satellite algorithm does not considerably affect the comparison. However, because of the lack of in situ measurements, it is difficult to clearly identify (i) where and when the satellite estimates are wrong and (ii) when and why the models fail knowing that the biases may depend on several errors or feedback.

4.1 Some limitations in the remote sensing algorithms

A well-known limitation of spaceborne microwave data is the large field of view of the sensors (being of the order of several tens of km, depending on the frequency). This may be responsible for biases along the ice sheet margin where the microwave signal could be affected by the tundra or sea surrounding the ice or when the ablation zone is very narrow. The increase in microwave emissivity measured by the radiometer when melting occurs may be significantly reduced if a pixel combines both melting and no-melting areas. As considerable melting occurs in these areas we have decided no to remove these pixels from the satellite-models comparison. We have only removed pixels near open water (ocean, fjord) as explained in Sect. 2.

The XPGR algorithm detects less melt days (about 10%) compared to ImpXPGR and ExtXPGR (see Fig. 6). This difference is clearly visible along the ice sheet margin where the probability that XPGR is biased by rainfall events or by the presence of clouds with liquid water is high. Figure 3 and Table 3 show that XPGR is less adequate than T19Hmelt or ExtXPGR to detect melt in the low elevation part of ablation zone where the probability to have rainfall events is the highest but where the probability to have melt is also the highest. Finally, Fig. 5 shows that the differences between XPGR and ExtXPGR occur mainly before August because the most of precipitation is solid after Mid-August.

TCD
4, 2433–2473, 2010

Both RCMs simulate less melt (about 20 melt days) along the eastern and south-eastern mountainous regions of the ice sheet than the microwave-derived estimates (see Fig. 6). Possibly, microwave brightness temperatures could be biased by rock outcrops found in these regions as suggested by Torinesi et al. (2003) in the Antarctic Peninsula and therefore, the remote sensing algorithms may overestimate melting over this area.

4.2 Biases in the models

Maximum melt extent area for the melt threshold using the meltwater produced by day (resp. LWC) occurs, on the average, during mid-July. The timing of this maximum is well reproduced by both models (see Fig. 5). However, from May to mid-June (resp. in July), RACMO2 underestimates (resp. overestimates) the melt area with respect to both satellite-based melt retrieval algorithms. The largest bias in MAR occurs in July when MAR underestimates the melt area if the meltwater production is used as melt threshold in the passive microwave data.

Figure 7 shows that MAR, compared to RACMO2, predicts more incoming longwave radiation in winter and less in summer. Compared to K-Transect measurements (West Greenland), RACMO2 tends to underestimate the longwave radiation, mainly in winter (Ettema et al., 2010). This suggests that MAR underestimates even more the longwave radiation in summer. Shortwave incoming fluxes are higher ($\sim$+5–10 W m^{-2}) in RACMO2 than in MAR before June and lower afterward. The differences are however negligible compared to the absolute values of the longwave fluxes driving the seasonal variability of the net fluxes. Finally, large differences between MAR and RACMO2 occur in the surface albedo simulation because the density of the snow surface (which prescribes the albedo in RACMO2) varies more slowly than the surface snow grains morphological characteristics (which determines the albedo in MAR) (Lefebre et al., 2003). Therefore, the surface snow albedo decreases earlier in MAR at the end of the spring and reaches earlier the dry snow albedo at the beginning of the winter. Part of differences between MAR and RACMO2 values of albedo are however enhanced by the melt-albedo positive feedback.

TCD
4, 2433–2473, 2010

The comparison with satellite-derived melt extent time series and those obtained with the two model suggests that at the beginning of the melt season, the snow albedo parametrization used in RACMO2 is not sensitive enough to wet snow conditions compared to the one used in MAR (which agrees better than RACMO2 with the satellite data). In addition to differences in the surface albedo parametrization, the MAR infrared radiative surplus in winter favors also an earlier beginning of the ablation season because the snowpack is warmer in MAR at the end of spring than in RACMO2.

In July, RACMO2 overestimates (note that it is the opposite for MAR) the melt extent compared to the satellites, likely because the RACMO2 albedo is too low as already suggested in Ettema et al. (2010). The downward longwave underestimation in MAR explains likely the melt extent underestimation in July.

Differences in response time between the two albedo parametrization schemes were shown by Lefebre et al. (2003), concluding that the CROCUS albedo parametrization gives better results in MAR (trough comparison with measurements at ETH-Camp). In addition, the comparison with GC-net measurements in Table 1 shows that MAR underestimates slightly the near-surface temperature in summer and RACMO2 overestimates surface temperature with respect to GC-net measurements as also shown by Ettema et al. (2010). Therefore, it is hard to identify which modules in the models fail and both albedo parametrization and radiation schemes (based in MAR and RACMO2 on the ECMWF model) should be critically assessed using high quality measurements of the radiative budget of the atmosphere.

At the end of the melting season (mid-August to September), RACMO2 underestimates the melt area only if the LWC is used as melt threshold (Fig. 5). The LWC in RACMO2 is limited to 2% of open pore space while this is 6% in the MAR model. Excess liquid water directly runs off in both models. Therefore, at the end of the melting season, there is still liquid water in the MAR snowpack while most of the meltwater is already refrozen in RACMO2. This can be a reason why RACMO2 underestimates melt extent in August if LWC is used as melt threshold and also why the MAR snowpack is warmer (refreezing of the retained meltwater prevents initial winter cooling of

TCD
4, 2433–2473, 2010

the snow pack). However, a LWC maximum reaching 6% in MAR could be also too high as we can see after an early (June 1979, 1988) or late (September 1999, 2004) melt event (see supplementary material) when MAR overestimates the area where liquid water is present in the snowpack while no more melt is simulated and observed (see T19Hmelt) at the surface.

The patterns of differences between the RCMs and T19Hmelt are quite similar (see Fig. 6). Simulated melt extent is underestimated with respect to T19Hmelt along the south-eastern margin and overestimated over the rest of the melt area. The differences are small compared to differences with ExtXPGR. The main difference between MAR and RACMO2 occurs along the north-western coast where MAR overestimates melt extent while RACMO2 underestimates it with respect to T19Hmelt. The differences between the outputs of the two RCMs are further discussed in the following paragraph.

If we use the LWC as melt threshold, MAR overestimates the melt extent along the north-western coast and in South Greenland and underestimates it in West and North Greenland with respect to ExtXPGR. The RACMO2 biases compared to ExtXPGR are very different, with rather an overestimation in the North and in the interior of South Greenland. These discrepancies are mainly due to differences in the snow model and in the snowfall pattern, affecting the number of days when bare ice is present on the surface.

1. As discussed earlier, MAR identifies melting areas that are absent in RACMO2 after Mid-August, likely because the maximum LWC in MAR could be 3 times larger that in RACMO2. This also explains why MAR and RACMO2 outputs differ in South Greenland.

2. In addition to the presence of LWC, a pixel is considered as melting by XPGR if there is bare ice at the surface, even if this pixel is not melting. In the models, a pixel is assumed to be covered by bare ice if the density of the first layer in the snow model is higher than $900\,\mathrm{kg\,m^{-3}}$. Figure 8 shows that a large part of the discrepancies between MAR and RACMO2 in Fig. 6 are explained by the

TCD
4, 2433–2473, 2010

difference in the modeled number of pixels with bare ice at the surface. The appearance of bare ice in summer is conditioned mainly by winter snow accumulation (Fig. 8). Indeed, MAR simulates more pixels with bare ice in areas of the ablation zone along the west coast, where MAR simulates less solid precipitation than RACMO2. Summer snowfall also impacts melting by increasing the albedo for a short period after a snowfall event. Differences in snowfall likely explains why RACMO2 underestimates melt extent (compared to T19Hmelt) along the north-western ice sheet margin.

3. In the north, both modeled precipitation distributions are similar although MAR simulates less bare ice pixels. However, the smallest thickness for a new top layer in the snow model is 2 mm water equivalent (WE) in MAR and 6.5 cm WE in RACMO2. Therefore, RACMO2 needs 6.5 cm WE of fresh snow to create a new layer above bare ice, while a few mm of WE is enough in MAR to change a bare ice (and then melting) pixel to a non-melting pixel. This difference in the minimum layer thickness impacts mainly the results in the dry north where only a few snowfall events occur in summer. This explains also, in addition to the differences in the surface albedo parametrization, why the surface albedo reaches dry snow values at the end of the ablation season sooner in MAR than in RACMO2.

5 Interannual variability

According to previous studies (Fettweis et al., 2007; Mote, 2007; Tedesco et al., 2008), both microwave-derived and model-simulated melt extent show a significant (99% confidence level) positive trend of melt extent (Fig. 9). Since 1979, the annual cumulated melt extent area (i.e. the annual total sum of every daily ice sheet melt area) has doubled. Figure 10 shows that positive trends in melt extent occur everywhere in both the ablation and percolation zones. The slope of the trend in the case of the XPGR-based melt area (Fig. 9) is not significant, likely because rainfall (which perturbs the

TCD
4, 2433–2473, 2010

melt detection by XPGR) has also increased in summer over the period 1979–2009 (Fettweis et al., 2007).

According to both models and remote sensing algorithms, the maximum cumulated melt area occurs in 2007, followed by 1998. Low melt extent values occur in 1983 and 1992 after, respectively, the El Chichon and Mont Pinatubo eruptions. The agreement between RCMs and microwave-derived melt over the full spaceborne passive microwave period (see supplementary material) suggests that (i) using a linear regression to cross-calibrate the five sensors is sufficient to apply the same threshold through the whole period in Eq. (1), (ii) the modeled melt variability is good and then, (iii) that the RCMs can be used to estimate the melt extent prior to 1979. The RCMs show in Fig. 9 that

1. the cumulated melt extent has been decreasing since the end of the 1950's to reach its minimum at the beginning of the satellite period.
2. the cumulated melt extent of 1998, 2003, 2005 and 2007 are unprecedented in the last 50 years.
3. the cumulated melt extent of 2000's is two times larger than those in the 1970–1980's.
4. melting during the 1970's and the 1980's was comparable.
5. there is a period of 2–3 years (about 30 months) in the time series i.e. a summer with a high cumulated melt extent is mostly followed by a summer with less melt. A similar variability is found in the North Atlantic Oscillation (Nicolay et al., 2008) which is known to influence the summer temperature over the GrIS (Fettweis, 2007).

TCD
4, 2433–2473, 2010

6 Discussion and conclusion

Results from two RCMs are compared with microwave brightness temperature-based melt extent estimates with the objective to study the evolution of melting over the GrIS since 1958.

We selected two algorithms to retrieve melt extent from the spaceborne passive microwave data set. The first one, using a fixed threshold on the T19H brightness temperature (see Eq. 1), is especially sensitive to the production of surface and subsurface meltwater by day. The second one, based on the XPGR algorithm from Abdalati and Steffen (1997) (see Eq. 5), detects melt when liquid water is present in the snow pack. The time evolution of melt area over the GrIS through summer and the number of melt days compare very well with results from both models. The retrieving algorithms as well as the RCMs show a significant (p-value = 0.01) increase of the melt area over the GrIS since 1979. The models show that the recent cumulated melt extents are without precedent in the 50 last years and are two times larger that the ones from the 1980's.

The good agreement between remote sensing results and model outputs provide robustness to the melt retrieving algorithms and melt threshold used. This intercomparison also allowed us to highlight some biases in the models although part of discrepancies between satellite and model comes from the microwave data itself which is biased by the tundra or rock pixels nearby the ice sheet.

1. Biases in the response time to surface snow changes in the albedo parametrizations used by RACMO2 explains likely why RACMO2 underestimates the melt extent at the beginning of the melt season and overestimates it in July.

2. The longwave radiation should be increased in MAR in summer to correct the melt extent underestimation occurring in July.

3. The LWC in the RACMO2 snow model is currently limited to 2% (compared to 6% in the MAR model) which prevents melt detection at the end of the ablation

TCD
4, 2433–2473, 2010

season when freezing conditions occur at the surface and there is normally still liquid meltwater in the snow pack.

4. The minimum thickness of a new layer in the RACMO2 snow model is 6.5 cmWE, compared to 2 mmWE in the MAR model. This overestimates the pixels with bare ice in the ablation zones where few snowfall events occur in summer. Knowing that MAR underestimates the melt extent at the north of the ice sheet, the minimum layer thickness threshold should be increase to enhance the agreement with remote sensing data. In addition, a maximum LWC value of 6% in MAR likely overestimates the melt extent after high melt events. High quality snow observations, at several locations of ice sheet, could help for choosing the maximum LWC value in the snow pack.

5. The comparison with the LWC sensitive algorithms shows that there are some biases in both simulated precipitation patterns. The winter snowfall accumulation impacts the appearance of bare ice at the surface in summer which is detected as wet by the XPGR-based algorithms.

The good agreement between the RCM results and the microwave-derived melt extent suggests that the RCMs could be run in an assimilation mode, constrained by the spaceborne passive microwave data. Indeed, the snow pack properties of the pixels where RCM disagrees with the microwave-derived melt detection could be changed. For example, if the RCM has to detect melt and does not simulate it, the snowpack temperature could be increased to reach conditions more favorable to melt while the water mass is conserved. As future development, we could associate to each brightness temperature a meltwater threshold as in Table 4 and assimilate it in the model to improve the meltwater production simulation. This could have significant impact on the modeled meltwater run-off.

Moreover, this study has shown that large uncertainties remain in the modeled bare ice appearance at the surface while most of the meltwater run-off occurs on this area. Therefore, the MODIS-based albedo could be used for evaluating the bare ice zones

TCD
4, 2433–2473, 2010

in the models and afterward, for forcing the models in an assimilation mode. Knowing that the GrIS run-off variability is driven in a large part by the bare ice area variability, this assimilation should help to improve the matching with other satellite data sets (GRACE,...), with the objective to reduce the uncertainties of the current SMB model-based estimates.

Supplementary material related to this article is available online at: http://www.the-cryosphere-discuss.net/4/2433/2010/tcd-4-2433-2010-supplement.pdf.

Acknowledgements. Xavier Fettweis is a postdoctoral researcher of the Belgian National Fund for Scientific Research. Marco Tedesco's work was supported through the NSF Arctic Natural Sciences grant # 0909388 and the NASA Cryosphere Program.

References

Abdalati W., Steffen, K., Otto, C., and Jezek, K. C.: Comparison of brightness temperatures from SSMI instruments on the DMSP F8 and FII satellites for Antarctica and the Greenland ice sheet, Int. J. Remote Sens., 16(7), 1223–1229, 1995. 2441

Abdalati, W. and Steffen, K.: Snowmelt on the Greenland ice sheet as derived from passive microwave satellite data, J. Clim., 10, 165–175, 1997. 2435, 2437, 2440, 2446, 2447, 2454

Abdalati, W. and Steffen, K.: Greenland ice sheet melt extent: 1979–1999, J. Geophys. Res., 106, 33983–33988, 2001. 2435, 2436, 2437, 2439, 2440, 2441, 2446, 2461, 2466

Armstrong, R. L., Knowles, K. W., Brodzik, M. J., and Hardman M. A.: DMSP SSM/I Pathfinder daily EASE-Grid brightness temperatures, May 1987 to April 2009, Boulder, CO, USA: National Snow and Ice Data Center, Digital media and CD-ROM, 1994. 2437

Bingham, A. W. and Drinkwater, M. R.: Recent changes in the microwave scattering properties of the Antarctic ice sheet: Special section on emerging scatterometer applications, IEEE T. Geosci. Remote, 38(4), 1810–1820, 2000. 2442

Brodzik, M. J. and Armstrong, R. L.: Near-Real-Time DMSP SSM/I-SSMIS Pathfinder Daily

TCD
4, 2433–2473, 2010

EASE-Grid Brightness Temperatures, June 2009 to September 2009, Boulder, CO USA: National Snow and Ice Data Center, Digital media, 2008. 2437

Brun, E., David, P., Sudul, M., and Brunot, G.: A numerical model to simulate snowcover stratigraphy for operational avalanche forecasting, J. Glaciol., 38, 13–22, 1992. 2437

Ettema, J., van den Broeke, M. R., van Meijgaard, E., van de Berg, W. J., Bamber, J. L., Box, J. E., and Bales, R. C.: Higher surface mass balance of the Greenland ice sheet revealed by high-resolution climate modeling, Geophys. Res. Lett., 36, L12501, doi:10.1029/2009GL038110, 2009. 2434, 2436, 2437

Ettema, J., van den Broeke, M. R., van Meijgaard, E., van de Berg, W. J., Box, J. E., and Steffen, K.: Climate of the Greenland ice sheet using a high-resolution climate model - Part 1: Evaluation, The Cryosphere Discuss., 4, 561–602, doi:10.5194/tcd-4-561-2010, 2010. 2437, 2449, 2450

Fettweis, X., Gallée, H., Lefebre, L., and van Ypersele, J.-P.: Greenland surface mass balance simulated by a regional climate model and comparison with satellite derived data in 1990–1991, Clim. Dynam., 24, 623–640, doi:10.1007/s00382-005-0010-y, 2005. 2436, 2443

Fettweis, X., Gallée, H., Lefebre, L., and van Ypersele, J.-P.: The 1988–2003 Greenland ice sheet melt extent by passive microwave satellite data and a regional climate model, Clim. Dynam., 27(5), 531–541, doi:10.1007/s00382-006-0150-8, 2006. 2436, 2443, 2446, 2447, 2461

Fettweis, X., van Ypersele, J.-P., Gallée, H., Lefebre, F., and Lefebvre, W.: The 1979–2005 Greenland ice sheet melt extent from passive microwave data using an improved version of the melt retrieval XPGR algorithm, Geophys. Res. Lett., 34, L05502, doi:10.1029/2006GL028787, 2007. 2436, 2443, 2452, 2453

Fettweis, X.: Reconstruction of the 1979–2006 Greenland ice sheet surface mass balance using the regional climate model MAR, The Cryosphere, 1, 21–40, doi:10.5194/tc-1-21-2007, 2007. 2434, 2436, 2437, 2453

Fettweis, X., Hanna, E., Gallée, H., Huybrechts, P., and Erpicum, M.: Estimation of the Greenland ice sheet surface mass balance for the 20th and 21st centuries, The Cryosphere, 2, 117–129, doi:10.5194/tc-2-117-2008, 2008. 2435

Fettweis X., Mabille G., Erpicum M., Nicolay, S., and van den Broeke M.: The 1958–2009 Greenland ice sheet surface melt and the mid-tropospheric atmospheric circulation, Clim. Dynam., doi:10.1007/s00382-010-0772-8, 2010. 2436, 2437

Gallée, H. and Schayes, G.: Development of a three-dimensional meso-γ primitive equations

TCD
4, 2433–2473, 2010

model, Mon. Weather Rev., 122, 671–685, 1994. 2436
Greuell, W. G. and Konzelmann, T.: Numerical modelling of the energy balance and the englacial temperature of the Greenland Ice Sheet. Calculations for the ETH-Camp location (West Greenland, 1155 m a.s.l.), Glob. Planet. Change, 9, 91–114, 1994. 2437
Joshi, M., Merry, C. J., Jezek, K. C., and Bolzan, J. F.: An edge detection technique to estimate melt duration, season and melt extent on the Greenland Ice Sheet using Passive Microwave Data, Geophys. Res. Lett., 28(18), 3497–3500, 2001. 2438
Hall, D. K., Williams, R. S., Luthcke, S. B., and Digirolamo, N. E.: Greenland ice sheet surface temperature, melt and mass loss: 2000–2006, J. Glaciol., 54(184), 81–93, 2008. 2434
Hanna, E., Huybrechts, P., Steffen, K., Cappelen, J., Huff, R., Shuman, C., Irvine-Fynn, T., Wise, S., and Griffiths, M.: Increased runoff from melt from the Greenland Ice Sheet: a response to global warming, J. Climate, 21, 331–341, 2008. 2434
Knowles, K., Njoku, E., Armstrong, R., and Brodzik, M. J.: Nimbus-7 SMMR Pathfinder Daily EASE-Grid Brightness Temperatures [CD-ROM], Natl. Snow and Ice Data Cent., Boulder, Colo, 2002. 2437
Lefebre, F., Gallée, H., van Ypersele, J., and Greuell, W.: Modeling of snow and ice melt at ETH-camp (west Greenland): a study of surface albedo, J. Geophys. Res., 108(D8), 4231, doi:10.1029/2001JD001160, 2003. 2437, 2449, 2450
Liu, H., Wang, L., and Jezek, K. C.: Spatiotemporal variations of snowmelt in Antarctica derived from satellite scanning multichannel microwave radiometer and Special Sensor Microwave Imager data (1978–2004), J. Geophys. Res., 111, F01003, doi:10.1029/2005JF000318, 2006. 2438, 2441
Mote, T. L. and Anderson, M. R.: Variations in snowpack melt on the Greenland ice sheet based on passive-microwave measurements, J. Glaciol., 41, 51–60, 1995. 2442
Mote, T. L.: Greenland surface melt trends 1973–2007: Evidence of a large increase in 2007, Geophys. Res. Lett., 34, L22507, doi:10.1029/2007GL031976, 2007. 2434, 2435, 2439, 2443, 2452
Nicolay, S., Mabille, G., Fettweis, X., and Erpicum, M.: 30 and 43 months period cycles found in air temperature time series using the Morlet wavelet method, Clim. Dynam., 33(7–8), 1117–1129, doi:10.1007/s00382-008-0484-5, 2008. 2453
Picard, G. and Fily, M.: Surface melting observations in Antarctica by microwave radiometers: correcting 26-year long time series from changes in acquisition hours, Remote Sens. Environ., 104(3), 325–336, 2006. 2435, 2439, 2440, 2441, 2442, 2465

TCD
4, 2433–2473, 2010

Steffen, K. and Box, J. E.: Surface climatology of the Greenland ice sheet: Greenland Climate Network 1995–1999, J. Geophys. Res., 106(D24), 33951–33964, 2001. 2442, 2444, 2445
Ulaby, F. and Stiles, W.: The active and passive microwave response to snow parameters. 2: water equivalent of dry snow, J. Geophys. Res., 85, 1045–1049, 1980. 2435
Tedesco, M.: Snowmelt detection over the Greenland ice sheet from SSM/I brightness temperature daily variations, Geophys. Res. Lett., 34, L02504, doi:10.1029/2006GL028466, 2007. 2435, 2438, 2441
Tedesco, M., Serreze, M., and Fettweis, X.: Diagnosing the extreme surface melt event over southwestern Greenland in 2007, The Cryosphere, 2, 159–166, doi:10.5194/tc-2-159-2008, 2008. 2434, 2452
Tedesco, M.: Assessment and development of snowmelt retrieval algorithms over Antarctica from K-band spaceborne brightness temperature (1979–2009), Remote Sens. Environ., 113(5), 979–997, 2009. 2439
Tedesco, M., Reichle, R., Loew, A., Markus, T., and Foster, J. L.: Dynamic Approaches for Snow Depth Retrieval From Spaceborne Microwave Brightness Temperature, IEEE T. Geosci. Remote, 48(4), 1955–1967, 2010. 2441
Torinesi, O., Fily, M., and Genthon, C.: Variability and trends of the summer melt period of Antarctic ice margin since 1980 from microwave sensors, J. Climate, 16, 1047–1060, 2003. 2439, 2444, 2449
Van den Broeke, M. R., Bamber, J., Ettema, J., Rignot, E., Schrama, E., van de Berg, W. J., van Meijgaard, E., Velicogna, I., and Wouters, B.: Partitioning recent Greenland mass loss, Science, 326, 984–986, 2009. 2434
Wake, L. M., Huybrechts, P., Box, J. E., Hanna E., Janssens, I., and Milne, G. A.: Surface mass-balance changes of the Greenland ice sheet since 1866, Ann. Glaciol., 50(50), 178–184, 2009. 2435
Wouters, B., Chambers, D., and Schrama, E. J. O.: GRACE observes small-scale mass loss in Greenland, Geophys. Res. Lett., 35, L20501, doi:10.1029/2008GL034816, 2008. 2434, 2435
Zwally, H. J. and Fiegles, S.: Extent and duration of Antarctic surface melting, J. Glaciol., 40(136), 463–476, 1994. 2439, 2442, 2465
Zwally, J. H., Giovinetto, M., Li, J., Cornejo, H., Beckley, M., Brenner, A., Saba, J., and Yi, D.: Mass changes of the Greenland and Antarctic ice sheets and shelves and contributions to sea-level rise: 1992–2002, J. Glaciol., 51(175), 509–527, 2005. 2435

TCD
4, 2433–2473, 2010

Table 1. Mean (over the 1995–2005 summers) percentage of number of melt days at 10 GC-Net AWS's (where melt is observed) when the RCM and the observations are in agreement, when the RCM fails to detect melt and when RCM detects melt while the observations do not. Two approaches (explained in 2) are used for detecting melt in the RCM modeled time series. The location of the GC-Net AWS's is also listed. Finally, the mean modeled daily temperature bias (in °C) with respect to the GC-net measurements over the 1995–2005 summers is also given.

ID	Name	Location	MAR (bias)	MAR (temp)	MAR (Melt)	RAC (bias)	RAC (temp)	RAC (melt)
1	Siss Camp	69.6° N, 49.2° W, 1149 m	+0.1 ± 0.3	90-4-6	84-2-14	+0.2 ± 0.2	89-6-5	85-9-6
2	CP1	69.9° N, 47.0° W, 2022 m	+0.0 ± 0.5	97-2-1	95-2-2	+1.9 ± 0.4	96-1-3	94-2-4
3	NASA-U	73.9° N, 49.5° W, 2368 m	+1.1 ± 1.6	100-0-0	100-0-0	+2.4 ± 1.5	100-0-0	100-0-0
4	GITS	77.1° N, 61.1° W, 1887 m	−0.5 ± 1.1	100-0-0	100-0-0	+0.9 ± 1.0	99-0-0	100-0-0
5	Humboldt	78.5° N, 56.8° W, 1995 m	−0.6 ± 0.7	100-0-0	99-0-0	+1.0 ± 0.4	100-0-0	100-0-0
7	Tunu-N	78.0° N, 34.0° W, 2020 m	−0.1 ± 0.4	100-0-0	100-0-0	+1.6 ± 0.3	99-0-0	100-0-0
8	DYE-2	66.5° N, 46.3° W, 2165 m	−0.6 ± 0.2	98-2-0	96-2-2	+1.3 ± 0.5	96-1-3	93-1-6
9	JAR1	69.5° N, 49.7° W, 962 m	+0.8 ± 0.3	90-3-7	83-2-16	+0.5 ± 0.4	89-4-7	87-5-8
10	Saddle	66.0° N, 44.5° W, 2559 m	−0.6 ± 0.3	99-1-0	99-1-1	+1.4 ± 0.3	99-0-1	98-0-2
12	NASA-E	75.0° N, 30.0° W, 2631 m	+0.2 ± 0.8	100-0-0	100-0-0	+1.7 ± 0.6	100-0-0	100-0-0
	Average		−0.0 ± 0.6	97-1-1	95-1-4	+1.3 ± 0.6	97-1-2	96-2-3

TCD
4, 2433–2473, 2010

Table 2. Abbreviation of the different techniques discussed in the text to detect the melt. The errors bar range is also listed.

Abrv.	Algorithm (Melt detected if...)	Errors
MAR/RACMO2 (temp)	Daily mean near-surface temperature >0 °C	
MAR/RACMO2 (Melt)	Daily meltwater production >8.5 mmWE	±0.75 mmWE
MAR/RACMO2 (LWC)	Daily mean liquid water content >1.2% in the top meter of snow	±0.1%
T19Hmelt	T19H >227.5 K	±2.5 K
XPGR	$\frac{T19H-T37V}{T19H+T37V} > XPGR_{thsd}$, see Abdalati and Steffen (2001)	±0.0025
ExtXPGR	XPGR or T19Hmelt	
ImpXPGR	XPGR + 4 corrections, see Fettweis et al. (2006)	

TCD
4, 2433–2473, 2010

Table 3. The same as Table 1 but with the T19H-based algorithms for different values of $T19H_{thsd}$. The best agreement is written in bold.

ID	Name	Location	$T19H_{thsd}$							XPGR
			215 K	220 K	225 K	227.5 K	230 K	235 K	240 K	
1	Siss Camp	69.6° N, 49.2° W, 1149 m	80-1-19	83-2-16	85-3-12	85-4-11	**86-5-9**	85-10-6	81-16-3	58-12-30
2	CP1	69.9° N, 47.0° W, 2022 m	90-1-10	92-1-8	93-1-6	94-1-5	95-1-4	96-2-2	**97-2-1**	88-2-10
3	NASA-U	73.9° N, 49.5° W, 2368 m	99-0-1	99-0-1	99-0-1	99-0-1	99-0-1	**100-0-0**	99-0-0	99-0-0
4	GITS	77.1° N, 61.1° W, 1887 m	99-0-0	99-0-0	99-0-0	99-0-0	**100-0-0**	100-0-0	100-0-0	100-0-0
5	Humboldt	78.5° N, 56.8° W, 1995 m	99-0-1	99-0-1	99-0-1	99-0-0	99-0-0	99-0-0	99-0-0	**100-0-0**
7	Tunu-N	78.0° N, 34.0° W, 2020 m	**100-0-0**	100-0-0	100-0-0	100-0-0	100-0-0	100-0-0	100-0-0	100-0-0
8	DYE-2	66.5°N, 46.3° W, 2165 m	91-0-8	93-1-7	95-1-5	95-1-4	96-1-3	**96-2-2**	96-2-2	90-2-8
9	JAR1	69.5° N, 49.7° W, 962 m	77-1-21	82-3-15	**83-7-10**	81-11-8	77-17-6	67-30-3	56-44-0	49-38-12
10	Saddle	66.0° N, 44.5° W, 2559 m	97-0-3	98-0-2	98-0-1	99-0-1	**99-0-1**	99-1-1	99-1-0	98-1-2
12	NASA-E	75.0° N, 30.0° W, 2631 m	**100-0-0**	100-0-0	100-0-0	100-0-0	100-0-0	100-0-0	100-0-0	100-0-0
	Average		93-0-6	94-1-5	**95-1-4**	**95-2-3**	**95-3-2**	94-4-1	93-7-1	88-6-6

TCD
4, 2433–2473, 2010

Table 4. Correspondence between Eq. (1)-based and RCM-based melt detection. The mean number of GrIS pixels when both RCM and T19H-based algorithms detect melt (RCM = SAT), when RCM detects melt and not the retrieving algorithms (RCM > SAT) and when RCM does not detect melt and well the T19H-based algorithms (RCM < SAT) is also listed in percent over the number of GrIS pixels × summer days. The remaining percent correspond to days where both RCM and T19H-based algorithms do not detect melt. The statistics (i.e. the mean correlation coefficient (Corr.) as well as the mean Root Mean Square Error (RMSE) over 1979–2009) between MAR/RACMO2 and the T19H-based GrIS melt extent time series are also listed.

$T19H_{thsd}$	melt threshold	MAR = SAT	>SAT	<SAT	RMSE	Corr.	RACMO2 = SAT	>SAT	<SAT	CRMSE	Corr.
215 K	5.00 mmWE	5.9	2.3	2.7	3.1	0.94	6.0	2.6	2.5	3.4	0.94
217.5 K	5.50 mmWE	5.3	2.2	2.5	3.0	0.94	5.5	2.5	2.3	3.3	0.94
220 K	6.25 mmWE	4.8	2.0	2.3	2.9	0.93	4.9	2.3	2.2	3.1	0.94
222.5 K	7.00 mmWE	4.2	1.9	2.1	2.8	0.93	4.3	2.1	2.1	3.0	0.93
225 K	7.75 mmWE	4.0	1.8	2.0	2.7	0.92	3.7	2.0	2.0	2.9	0.92
227.5 K	8.50 mmWE	3.3	1.8	1.8	2.6	0.92	3.1	1.8	1.9	2.8	0.91
230 K	9.25 mmWE	2.8	1.8	1.7	2.6	0.91	2.6	1.7	1.8	2.7	0.90
235 K	11.00 mmWE	1.9	1.8	1.3	2.4	0.87	1.6	1.6	1.5	2.4	0.86

TCD
4, 2433–2473, 2010

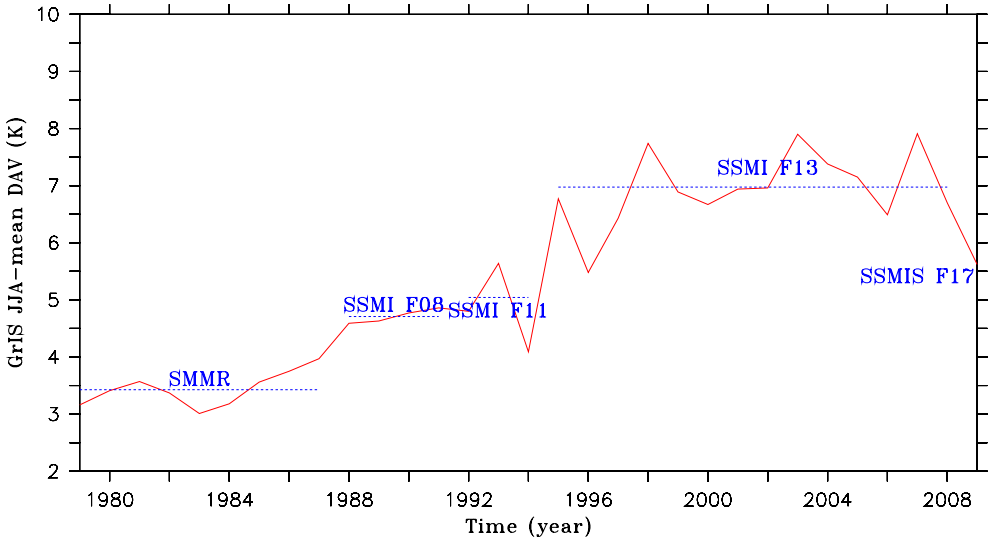

Fig. 1. Time series of the GrIS June–July–August (JJA) mean of DAV for the five satellites of the spaceborne passive microwave data set. In dashed blue, there is the average over the period covered by the four microwave satellites.

TCD
4, 2433–2473, 2010

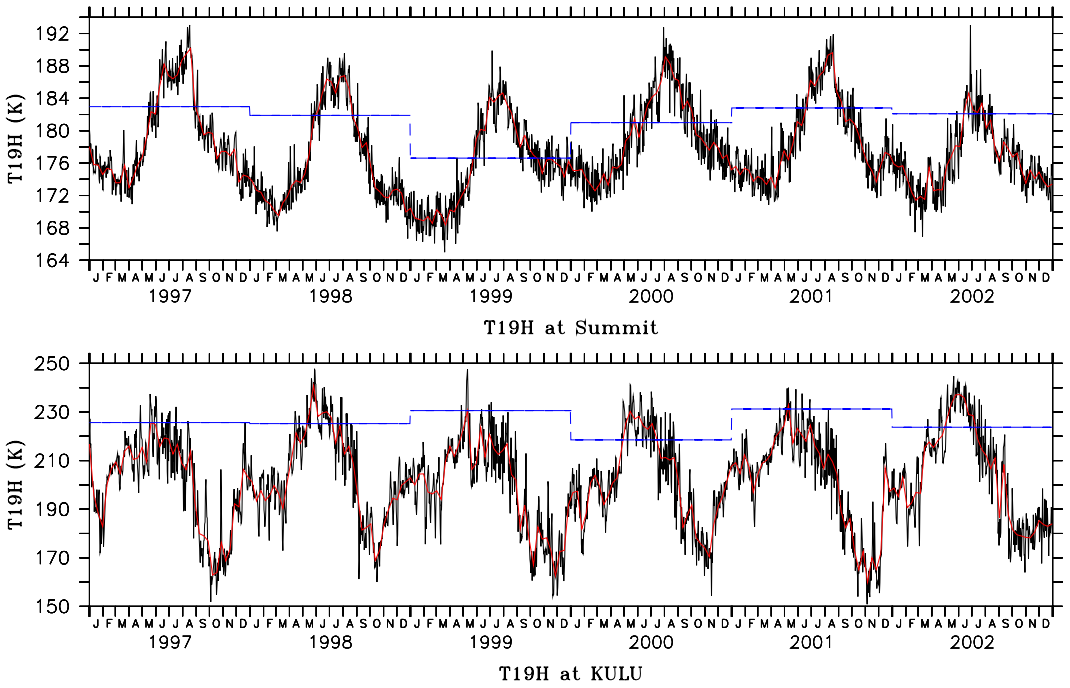

Fig. 2. The T19H time series for a cold area of the ice sheet (near Summit: 72.4° N, 37.4° W, 3250 m) and for a warmer area along the east coast (near KULU: 65.8° N, 39.6° W, 878 m). In red, the 10-day running mean. The annual threshold $T19H_{thsd}$ using the approach of Picard and Fily (2006) for Summit and using the approach of Zwally and Fiegles (1994) for KULU is plotted in dashed blue.

TCD
4, 2433–2473, 2010

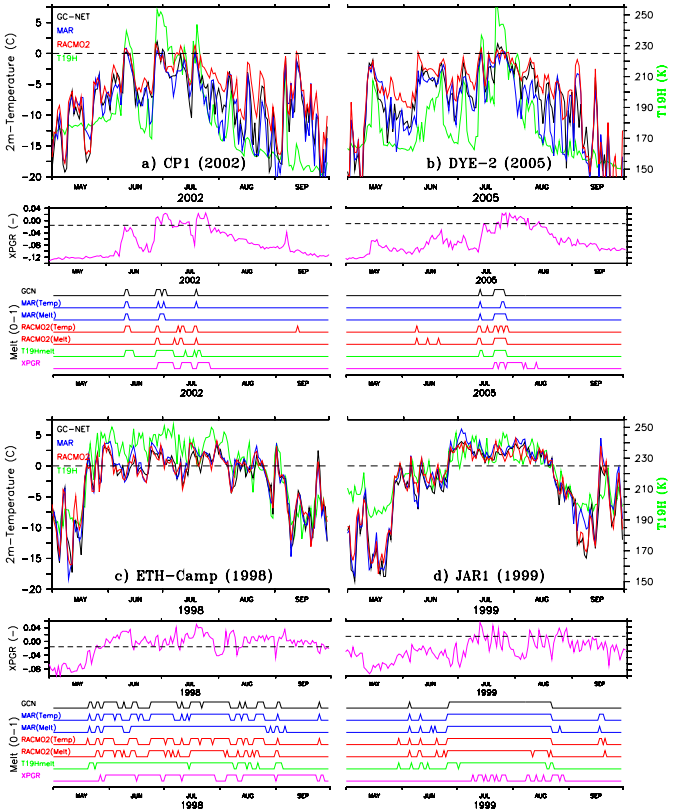

Fig. 3. **(a)** Top – Daily mean near-surface temperature (in black) observed in summer 2002 at Crawford Point 1 (69.9° N, 47° W, 2022 m), 3 m-temperature simulated by the MAR model (in blue), 2 m-temperature simulated by the RACMO2 model (in red) and, the T19H brightness temperature (in green on the left axe) for the pixel nearest CP1. Middle – the XPGR value as defined by Abdalati and Steffen (2001). The dotted line shows the XPGR threshold value used by Abdalati and Steffen (2001) for melt detection. Below – The Melt/no melt time series derived from observation (daily mean temperature ≥0 °C), simulated by the RCMs (see Table 2), derived from the T19H temperature by using Eq. 1 and using the XPGR algorithm. **(b)** The same as (a) but for DYE-2 (66.5° N, 46.3° W, 2165 m) in 2005. **(c)** The same as (a) but for ETH-Camp (69.6° N, 49.2° W, 1149 m) in 1998. **(d)** The same as (a) but for JAR-1 (69.5° N, 49.6° W, 962 m) in 1999.

TCD
4, 2433–2473, 2010

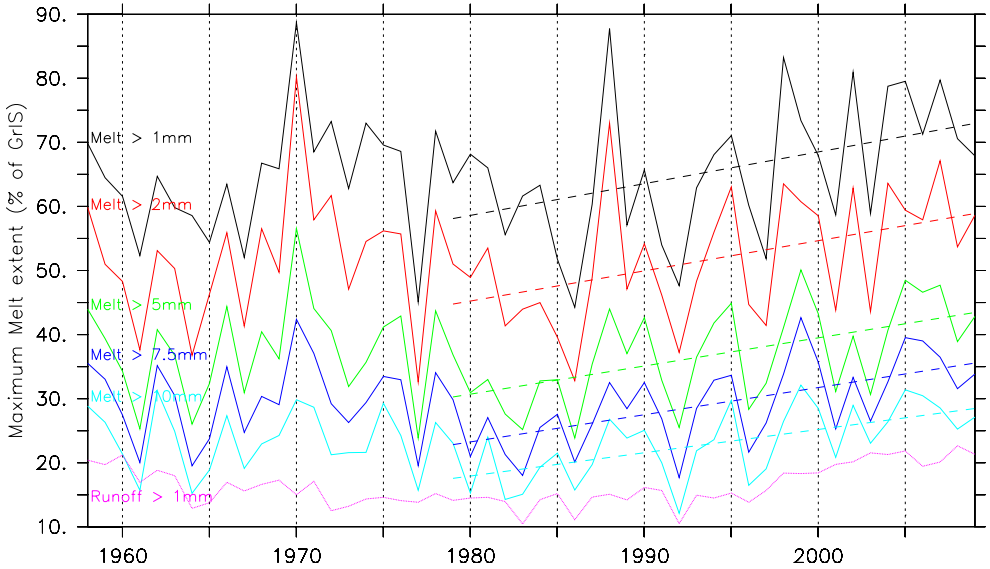

Fig. 4. Time series of the maximum melt extent (in percentage of the GrIS area) simulated by MAR for different melt thresholds: daily meltwater production higher than 1, 2, 5, 7.5 and 10 mmWE and daily runoff higher than 0 mmWE. Finally, the linear trend over 1979–2009 is given in dashed line.

TCD
4, 2433–2473, 2010

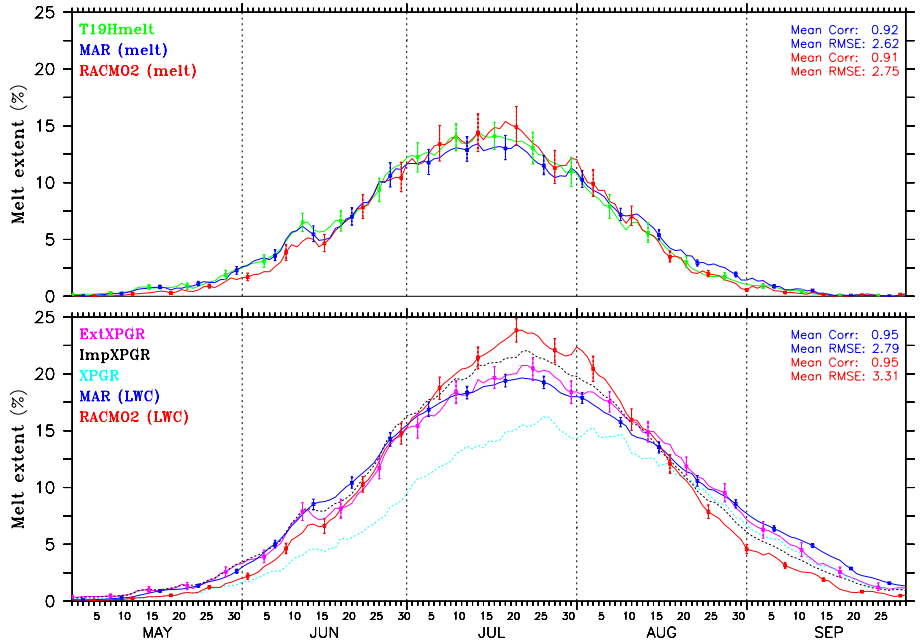

Fig. 5. Average daily seasonal cycle (1979–2009) of melt area (in % of GrIS area) simulated by MAR and RACMO2 as well as retrieved from the spaceborne passive microwave data set with the different techniques discussed in the text (see 2). The error bars show a positive/negative change of the threshold used to derive the melt extent as listed in Table 2. The statistics (i.e. the mean correlation coefficient as well as the mean Root Mean Square Error over 1979–2009) between MAR (in blue)/RACMO2 (in red) and the T19Hmelt (resp. ExtXPGR) algorithms are also listed.

TCD
4, 2433–2473, 2010

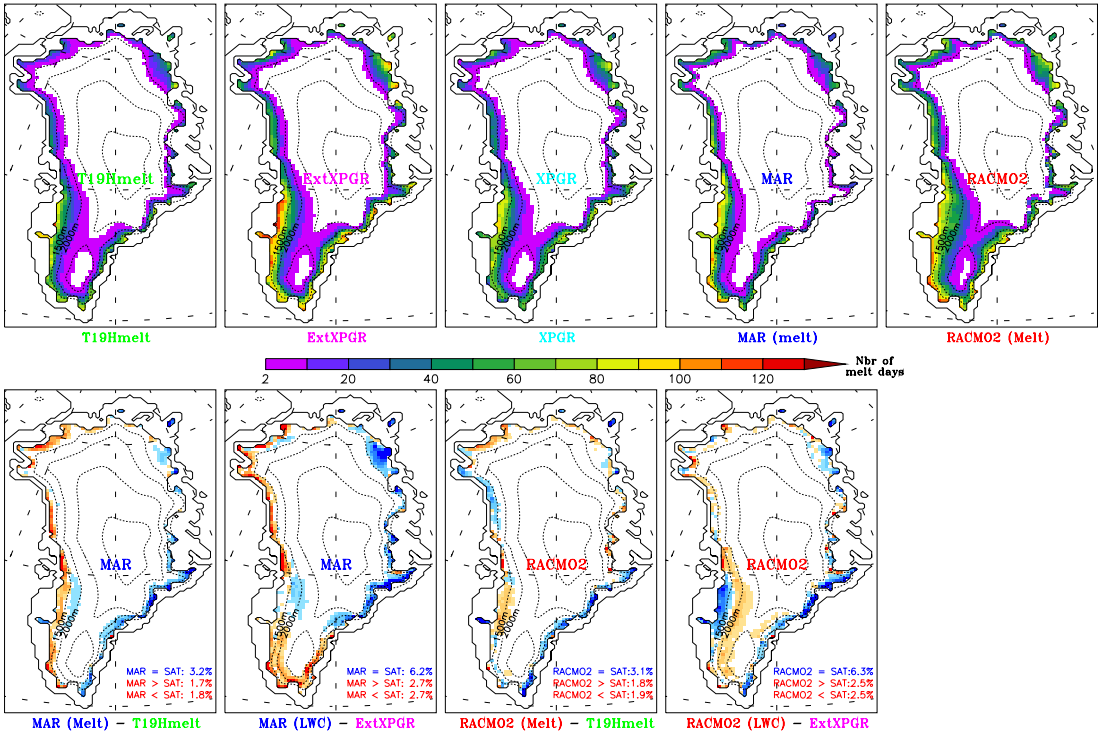

Fig. 6. Top – Annual mean total number of melt days derived from the spaceborne passive microwave data and simulated by the RCMs using algorithms described in Table 2. Below – The difference between models and the T19Hmelt and ExtXPGR algorithms. The mean number of GrIS pixels when RCM and the algorithms detect melt (RCM = SAT), when RCM detects melt but the retrieving algorithms do not (RCM > SAT) and when RCM does not detect melt while the algorithms do (RCM < SAT) is also listed as a percentage of the number of GrIS pixels × summer days.

TCD
4, 2433–2473, 2010

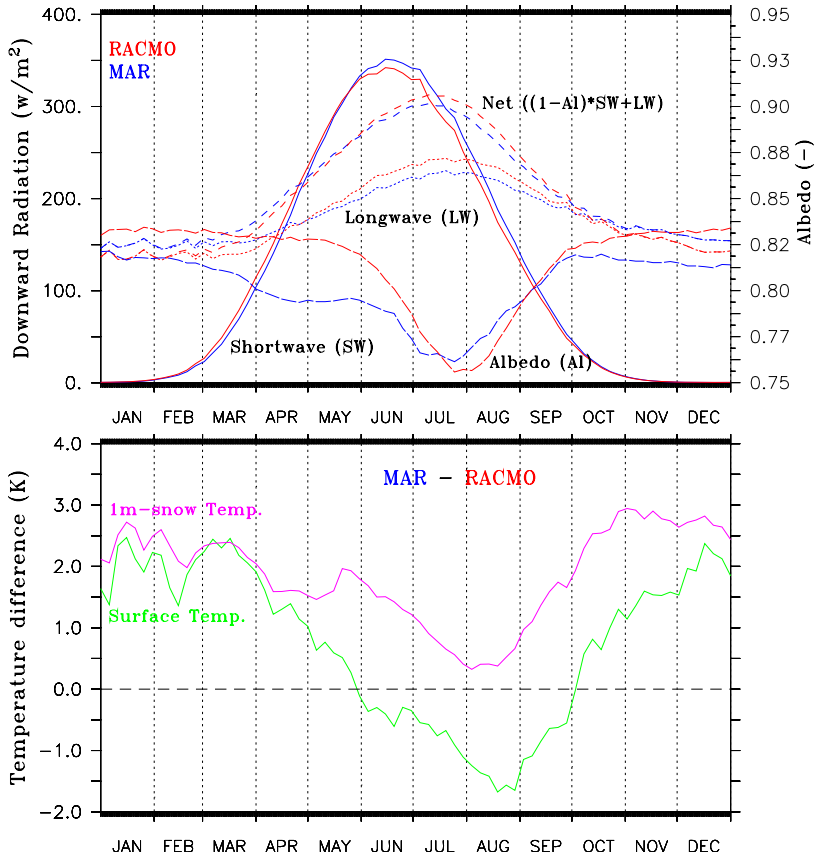

Fig. 7. Top – Time series of the mean shortwave (solid line), longwave (dotted line), albedo (dashed line on right y-axis) and net radiation (dashed line) averaged over the melting zone of the GrIS (i.e. surface height below 2500 m) and over the period 1979–2009 simulated by MAR (in blue) and by RACMO2 (in red). Below) Time series of the mean difference in surface temperature (resp. the temperature of the top meter of snow) between MAR and RACMO2.

TCD
4, 2433–2473, 2010

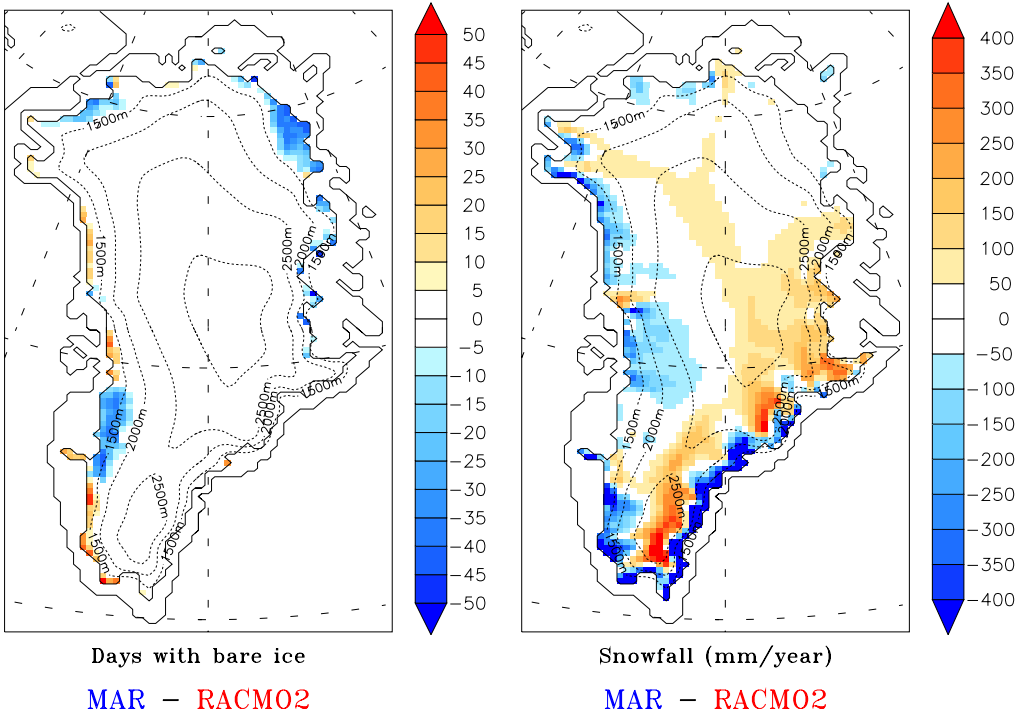

Fig. 8. Left – The mean difference of the number of days (per year) with bare ice at the surface simulated by MAR and by RACMO2. Right – The same but for the annual snowfall in mmWE.

TCD
4, 2433–2473, 2010

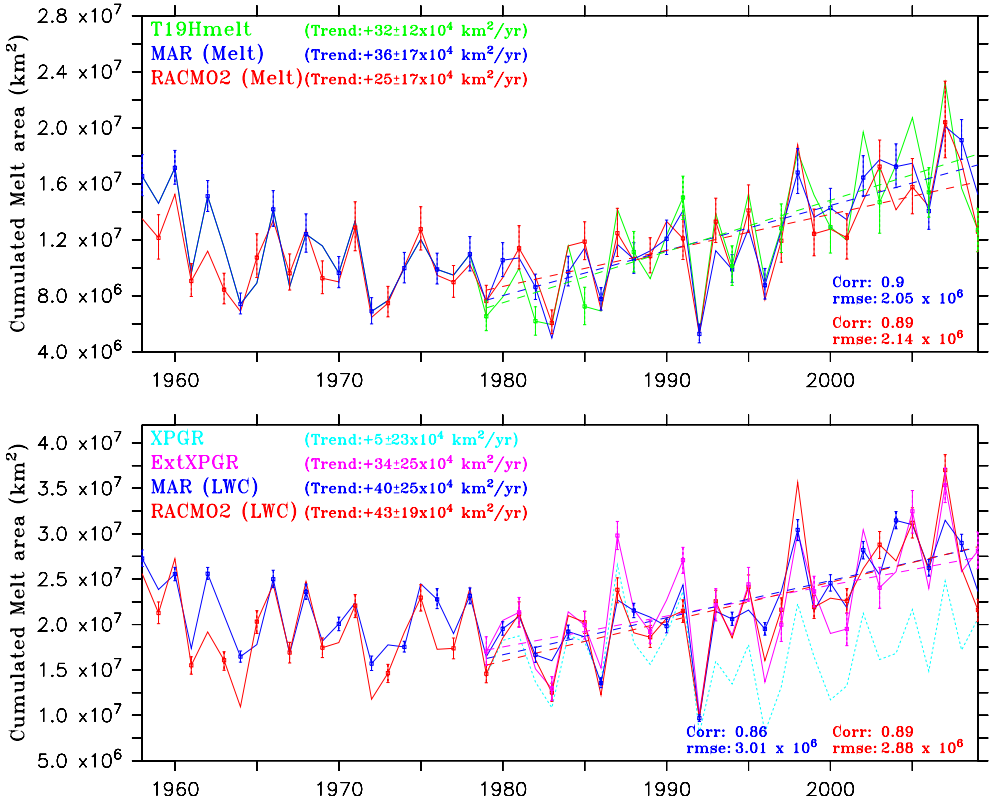

Fig. 9. Time evolution of the annual cumulated GrIS melt area simulated by the RCMs and retrieved from the spaceborne passive microwave data set with the different techniques discussed in the text (see 2). The cumulated melt area is defined as the annual total sum of every daily ice sheet melt area. The linear trend (in dashed line) as well as the error bars (see Table 2) are also shown. The uncertainty range of the trend denotes three standard deviations of the trend i.e. a significance of 99%.

TCD
4, 2433–2473, 2010

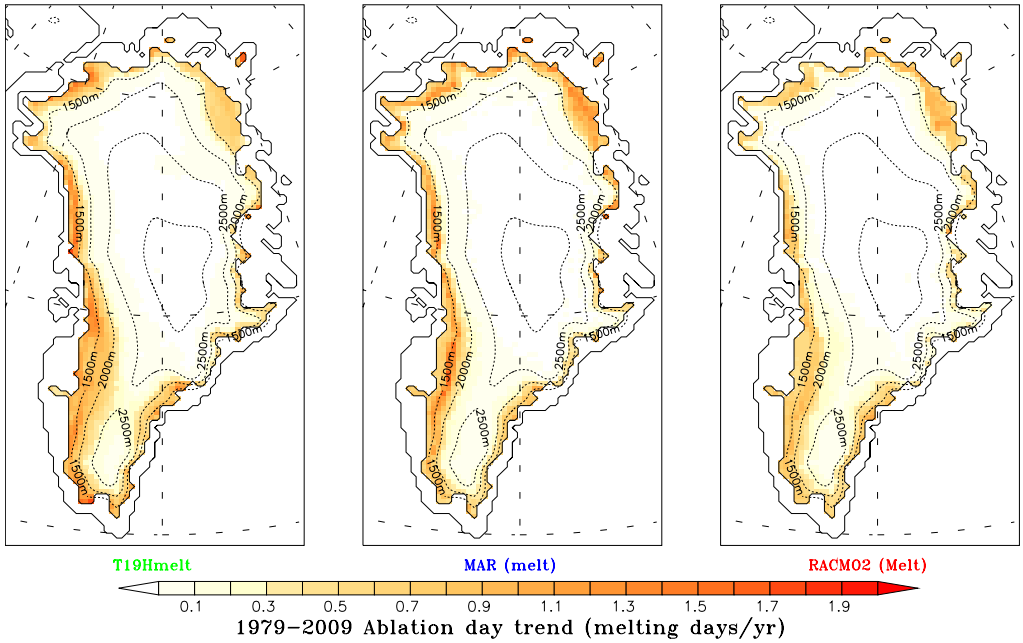

Fig. 10. Linear melt trend (in ablation days year^{-1}) detected by T19Hmelt and simulated by the models for the period 1979–2009.

TCD
4, 2433–2473, 2010